

On the origin of the X-rays and the nature of accretion in NGC 4261

M. Gliozzi¹, R.M. Sambruna¹, and W.N. Brandt²

¹ George Mason University, Dept. of Physics & Astronomy & School of Computational Sciences, 4400 University Drive, MS 3F3, Fairfax, VA 22030

² The Pennsylvania State University, Department of Astronomy & Astrophysics, 525 Davey Lab, University Park, PA 16802

Received: ; accepted:

Abstract. We report on the X-ray properties of the radio galaxy NGC 4261, combining information from the *XMM-Newton*, *Chandra*, and *BeppoSAX* satellites. Goals of this study are to investigate the origin of the X-rays from this low-power radio galaxy and the nature of the accretion process onto the central black hole. The X-ray spectrum of the nuclear source extending up to 100–150 keV is well described by a partially covered (covering factor > 0.8) power law with a photon index $\Gamma \simeq 1.5$ absorbed by a column density $N_{\text{H}} > 5 \times 10^{22} \text{ cm}^{-2}$. The X-ray luminosity associated with the non-thermal component is $\sim 5 \times 10^{41} \text{ erg s}^{-1}$. The nuclear source is embedded in a diffuse hot gas ($kT \sim 0.6 - 0.65 \text{ keV}$), whose density profile implies a Bondi accretion rate of $\sim 4.5 \times 10^{-2} M_{\odot} \text{ yr}^{-1}$. For the first time rapid X-ray variability is detected in a low-power radio galaxy at more than 99% confidence level. The observed X-ray spectral and variability properties indicate the accretion flow as the most likely origin of the bulk X-ray continuum. This conclusion is strengthened by energetic considerations based on a comparison between the X-ray luminosity and the kinetic power of the jet, which also suggest that the Bondi accretion rate overestimates the actual accretion rate onto the black hole.

Key words. Galaxies: active – Galaxies: nuclei – X-rays: galaxies

1. Introduction

One of the most interesting issues of extragalactic astrophysics is the condition of matter near black holes. The importance of this issue is stressed by the recent discovery from HST and ground-based observations that most nearby galaxies harbor supermassive black holes (e.g., Gebhardt et al. 2000, Ferrarese et al. 2001). Together with independent evidence that weak nuclear activity is common in both spirals and ellipticals (Low-Ionization Nuclear Emission-Line Regions, hereafter LINERs; e.g., Heckman 1980), this underlines a fundamental link between “normal” and active galaxies. Since accreting supermassive black holes are widely believed to be responsible for the nuclear activity in active galactic nuclei (AGN), one naturally wonders why intense activity is limited to a minority of galaxies. Inefficient accretion onto the central black hole is generally considered as the most likely explanation. This could be due either to radiatively inefficient advection (or convection) dominated accretion flows (e.g., Narayan 2002), or to unsteady feedback-modulated accretion (e.g., Binney & Tabor 1995, Ciotti & Ostriker

2001), which can stop or decrease to a low duty cycle the accretion onto the massive black hole.

Weak AGN may represent the link between powerful AGNs and “normal” galaxies. Therefore, an important role in understanding the nature of accretion around massive black holes can be played by the study of weak AGNs at X-ray energies, where the combination of spatial, spectral, and temporal analyses offer an ideal means by which we can understand the physics of their central engines and in particular the accretion process onto their black holes.

The nearby ($z=0.0074$) giant elliptical NGC 4261 (3C270) contains a supermassive black hole with $M_{\text{BH}} = (4.9 \pm 1.0) \times 10^8 M_{\odot}$ (Ferrarese, Ford, & Jaffe 1996). It is one of a handful of nearby early-type galaxies where low-luminosity nuclear activity is detected. It is classified as a Fanaroff-Riley I (FR I) radio galaxy, with a compact core and twin jets extending E-W, oriented at $\theta = (63 \pm 3)^{\circ}$ with respect to the line of sight (Piner, Jones, & Wehrle 2001). Optical spectroscopy reveals a LINER in the nucleus of the galaxy (Ho, Filippenko, & Sargent 1995). *HST*/STIS ultraviolet images of NGC 4261 show the presence of a jet-like structure on pc scales with position angle consistent with the orientation of the radio and X-ray jets

(Chiaberge et al. 2003). In the X-ray band, diffuse thermal emission plus a non-thermal nuclear component is present at low energies in *ROSAT* images (Worrall & Birkinshaw 1994). More recently, *Chandra* spectral results have been reported by Chiaberge et al. (2003), showing a continuum described by a flat power law with photon index $\Gamma \sim 1.4$ and an excess column density of $N_H \sim 6 \times 10^{22} \text{ cm}^{-2}$. Marginal evidence for an unresolved Fe line was previously claimed from a 40 ks *ASCA* exposure (Sambruna, Eracleous, & Mushotzky 1999). These spectral properties and the presence of an unresolved Fe K line at 6.9 keV have been confirmed by Sambruna et al. (2003; hereafter Paper I) using *XMM-Newton* data, which also show evidence for significant variability on short time scales.

In this paper, we present a detailed study of the X-ray nuclear and circumnuclear properties of NGC 4261, combining the complementary capabilities of *XMM-Newton*, *Chandra*, and *BeppoSAX*. The main questions addressed in this study are 1) What is the origin of the X-ray emission from this galaxy? In particular, concerning the nuclear emission, are the bulk of the X-rays due to the inner jet or is the accretion process responsible for them? 2) What is the nature of the accretion process at work in the nucleus of NGC 4261?

In §2 we describe the observations and data reduction. In §3 we perform a spatial analysis of the circumnuclear region utilizing *Chandra* data. In §4 and §5 we carry out temporal and spectral analyses, respectively. In §6 we discuss the nuclear properties inferred from the X-ray data and compare them with the jet properties on pc scales derived from radio observations. Finally, in §7, we summarize the main conclusions. Throughout the paper we use a Friedman cosmology with $H_0 = 75 \text{ km s}^{-1} \text{ Mpc}^{-1}$ and $q_0 = 0.5$. With these cosmological parameters, $1'' = 141 \text{ pc}$ at the distance of NGC 4261.

2. Observations and data reduction

Table 1 summarizes the X-ray observations of NGC 4261 carried out with *Chandra*, *BeppoSAX*, and *XMM-Newton*. The background-subtracted count rates are given in column 5. Details are given below for each satellite.

2.1. *XMM-Newton*

We observed NGC 4261 with *XMM-Newton* on 2001 October 16 for a duration of ~ 27 ks with the EPIC pn, and for ~ 32 ks with EPIC MOS1 and MOS2. All of the EPIC cameras were operated in full-frame mode with a medium filter. The recorded events were reprocessed and screened with the latest available release of the *XMM-Newton* Science Analysis Software (SAS 5.3.3) to remove known hot pixels and other data flagged as bad; only data with FLAG=0 were used. Investigation of the full-field light curves revealed the presence of two periods of background flaring; these events were screened reducing the effective total exposures to ~ 21 ks for the EPIC pn and ~ 26 ks for the MOS cameras. Background data were extracted

from source-free circular regions on the same chips containing the source. There are no signs of pile-up in the pn or MOS cameras according to the SAS task `epatplot`. With an extraction radius of $20''$ the detected count rates in the energy range 0.3–10 keV are $(9.52 \pm 0.20) \times 10^{-2} \text{ s}^{-1}$ for the MOS1, $(8.91 \pm 0.20) \times 10^{-2} \text{ s}^{-1}$ for the MOS2, and $(3.03 \pm 0.04) \times 10^{-1} \text{ s}^{-1}$ for the pn.

The spectra were rebinned such that each spectral bin contains at least 20 counts in order to apply χ^2 minimization, and fitted using the XSPEC v.11 software package (Arnaud 1996). The quoted errors on the derived best-fitting model parameters correspond to a 90% confidence level for one interesting parameter (i.e., a $\Delta\chi^2 = 2.7$ criterion) unless otherwise stated. The latest publicly available responses were used. The same procedure was applied to the *Chandra* and *BeppoSAX* data.

2.2. *Chandra*

NGC 4261 was observed with *Chandra* on 2000 May 6. The observations were carried out in a subarray mode (frame-time ~ 1.8 s) to minimize the possible pile-up of the nucleus. The data reduction was performed with CIAO v. 2.3 and CALDB v. 2.18. The data were reprocessed with `acis_process_events` and screened to exclude periods of flaring background, reducing the effective exposure to ~ 32 ks. In order to take into account the continuous degradation of the ACIS quantum efficiency (QE) due to molecular contamination of the optical blocking filters, we applied ACISABS¹ to the ancillary response function (ARF) file. The S3 background-subtracted count rate in the 0.35–9 keV energy band is $(7.04 \pm 0.15) \times 10^{-2} \text{ cts s}^{-1}$.

2.3. *BeppoSAX*

BeppoSAX observed NGC 4261 with the Narrow Field Instruments, LECS (0.1–4.5 keV) and MECS (1.3–10 keV), and with the PDS (15–220 keV) on 2000 December 27, with effective exposures of 19.6 ks, 67.4 ks, and 32.6 ks, respectively. The LECS and MECS are imaging instruments, while the PDS is a phoswich detector system. The observations were performed with 2 active MECS units. Standard data reduction techniques were employed, following the prescription given by Fiore et al. (1999). LECS and MECS spectra and light curves were extracted from regions with radii of $4'$ and $2'$, respectively, in order to maximize the accumulated counts at both low and high energies. An inspection of the MECS f.o.v. argues against the presence of confusing bright sources in the PDS data. Background spectra were extracted from high Galactic latitude “blank” fields, whereas for the light curves a source-free region in the field of view was used. The background-subtracted count rates are $(9.9 \pm 0.8) \times 10^{-3} \text{ cts s}^{-1}$ for the LECS in the 0.1–4.5 keV band, $(8.5 \pm 0.4) \times 10^{-3} \text{ cts s}^{-1}$

¹ see the Chartas & Getman model description at www.astro.psu.edu/users/chartas/xcontdir/xcont.html

Table 1. X-ray observation log

Satellite	Instrument	Observation Date [yy/mm/dd]	Exposure [ks]	Count Rate [s ⁻¹]	Extraction Radius
<i>Chandra</i>	ACIS-S3	00/05/06	32.0 ^a	$(7.04 \pm 0.15) \times 10^{-2}$	2''
<i>BeppoSAX</i>	MECS23	00/12/27	67.4	$(8.51 \pm 0.39) \times 10^{-3}$	2'
<i>XMM-Newton</i>	EPIC pn	01/12/16	21.3 ^a	$(3.03 \pm 0.04) \times 10^{-1}$	20''

^a Effective exposure after excluding times of background flares.

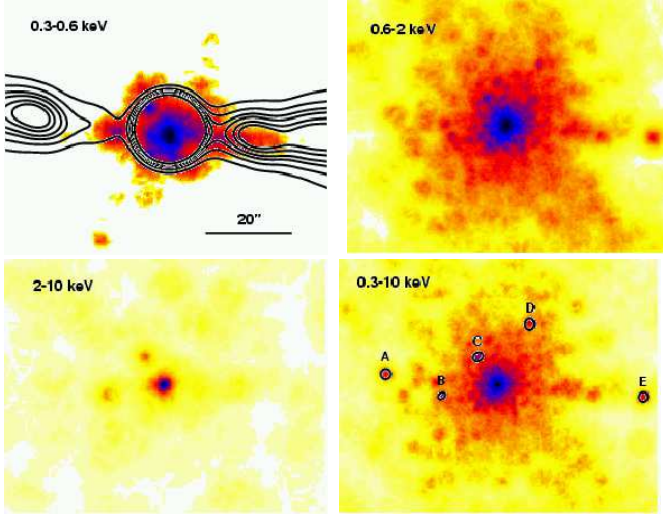


Fig. 1. *Chandra* ACIS-S3 adaptively smoothed images of NGC 4261 in different energy bands. The top left panel shows the emission in the ultrasoft range 0.3–0.6 keV, with VLA radio contours overlaid. The top right and bottom left panels display the soft (0.6–2 keV) and hard (2–10 keV) X-ray emission, respectively. In the bottom right panel the total emission (0.3–10 keV) is shown; the sources detected with *wavdetect* are marked. At the distance of NGC 4261, 20'' corresponds to a distance of 2.8 kpc. North is up, and East to the left.

for the MECS in the 2–10 keV band, and $(6.9 \pm 3.6) \times 10^{-2}$ cts s⁻¹ for the PDS in the 15–150 keV energy band.

3. Spatial Analysis

With its subarcsecond spatial resolution, *Chandra* provides us with the opportunity to take a direct look at the faint nuclear emission and to disentangle the different X-ray components in NGC 4261. Figure 1 shows four adaptively smoothed images of NGC 4261 in different energy bands as seen by ACIS-S3. In the ultrasoft range (0.3–0.6 keV, top left panel), the X-ray emission is preferentially distributed along the jet direction indicated by the VLA radio contours superimposed. It is worth noticing that *Chandra* detects an X-ray jet on kpc scales, i.e., on scales larger than the jet-like feature observed in the

UV ($\sim 20 \times 60$ pc; Chiaberge et al. 2003), and much larger than the VLBA radio jet ($\sim 1 \times 3$ pc; Piner et al. 2001).

In the 0.6–2 keV range (top right panel), the radiation is uniformly distributed on kpc scales (20'' corresponds to a distance of 2.8 kpc). The hard X-rays (2–10 keV, bottom left panel) are consistent with a point-like source. Finally, several point-like sources (bottom right panel) are found with *wavdetect* in the circumnuclear region of NGC 4261. Details about source detection and the serendipitous sources' properties are reported in the Appendix. Three of these sources are located within 20'' of the nucleus of NGC 4261 and therefore fall in the *XMM-Newton* extraction region. However, their contribution to the X-ray flux is negligible: the brightest source (source C) contributes only $\sim 3\%$ of the total counts, while the remaining sources contribute less than 1%.

A more quantitative method to derive information from the photon spatial distribution is to extract a radial profile. Using the *ciao* tools *dmextract* and *dmtcalc*, we extracted the azimuthally-averaged radial profile of the circumnuclear region out to 100'' (corresponding to ~ 14 kpc). A series of annular regions, with an increment of the radius of 2'', was used to extract the non-background-subtracted radial profile in the 0.3–2 keV range.

To determine the physical properties of the extended X-ray emission, we fitted the surface-brightness profile with a β -model (e.g., Cavaliere & Fusco-Femiano 1976) of the form

$$S(r) = S_0 \left(1 + \frac{r^2}{r_c^2} \right)^{-3\beta+1/2} \quad (1)$$

The energy-dependent PSF (see Donato et al. 2003 for details on its derivation) and the background were explicitly included in the fit. The result is shown in Figure 2.

The best-fit values ($\chi_{\text{red}}^2 = 1.2$, 46 d.o.f.) for the β -model are $S_0 = (6.5 \pm 0.3) \times 10^{-3}$ cts s⁻¹ arcsec⁻², $\beta = 0.53 \pm 0.01$, and $r_c = (1.40 \pm 0.06)''$. The quoted errors are 1σ . The value of β is consistent with typical values for gas confined in nearby elliptical galaxies (e.g., Forman et al. 1985). On the other hand, the core radius is considerably smaller than the value inferred from *ROSAT* PSPC data by Worrall & Birkinshaw (1994) with β fixed at 2/3. This is likely due to the different spatial resolutions of the two instruments: the *Chandra* ACIS-S with its subarcsecond resolution can resolve emission on very small

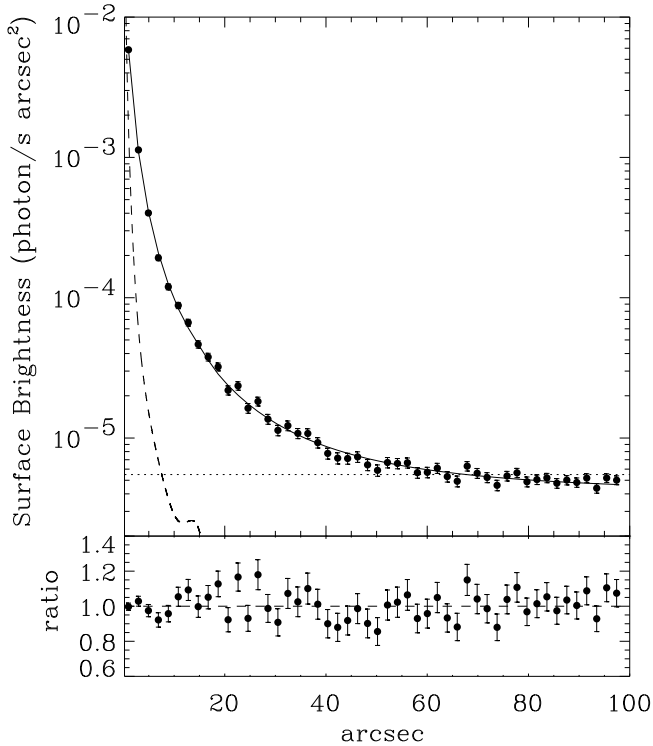


Fig. 2. *Chandra* ACIS-S3 azimuthally averaged surface brightness profile of NGC 4261. The solid line represents the β -model which best-fits the data, while the dashed and dotted lines represent the PSF and the background, respectively. The lower panel shows the data-to-model ratio. At the distance of NGC 4261, 100'' corresponds to a distance of ~ 14 kpc.

scales, whereas the *ROSAT* PSPC with a PSF FWHM of $\sim 25''$ can only detect extended emission on group scales.

The physical parameters of the extended emission can be obtained by de-projecting the surface-brightness profile. With this method we can derive the corresponding density profile (see, e.g., Ettori 2000):

$$n(r) = n_0 \left(1 + \frac{r^2}{r_c^2} \right)^{-\frac{3\beta}{2}} \quad (2)$$

This relation assumes isothermal, hydrostatic equilibrium in spherical symmetry. We adopted the cooling function value (e.g., Sarazin 1988) for the hot gas temperature and the abundances derived from the spectral analysis. The resulting central particle density is $n_0 = 0.17 \pm 0.01 \text{ cm}^{-3}$.

4. Temporal Analysis

As shown in Paper I, rapid variability is present in the nucleus of NGC 4261. To investigate further the short-term variability only EPIC pn data are useful. The reason why MOS data cannot increase the photon statistics is the following: the MOS cameras share with the Reflection Grating Spectrometers (RGS1 and RGS2, respectively) the focal planes of their respective X-ray telescopes. As

Table 2. Short-term X-ray variability of NGC 4261

Energy band	Radius	χ_{red}^2 (22 d.o.f.)	P_{χ^2}	F_{var}^a (%)
0.3–10 keV	10''	1.74	1.2%	6.7 ± 2.2
	20''	1.85	0.6%	5.7 ± 1.8
	30''	1.60	2%	4.4 ± 1.7
0.3–0.8 keV	20''	2.03	0.2%	8.9 ± 2.7
0.8–2 keV	20''	1.03	36%	3.0 ± 4.4
2–10 keV	20''	1.14	24%	6.8 ± 6.0

^a The errors on F_{var} are calculated as in Edelson et al. (2002) and should be considered conservative estimates of the true uncertainty.

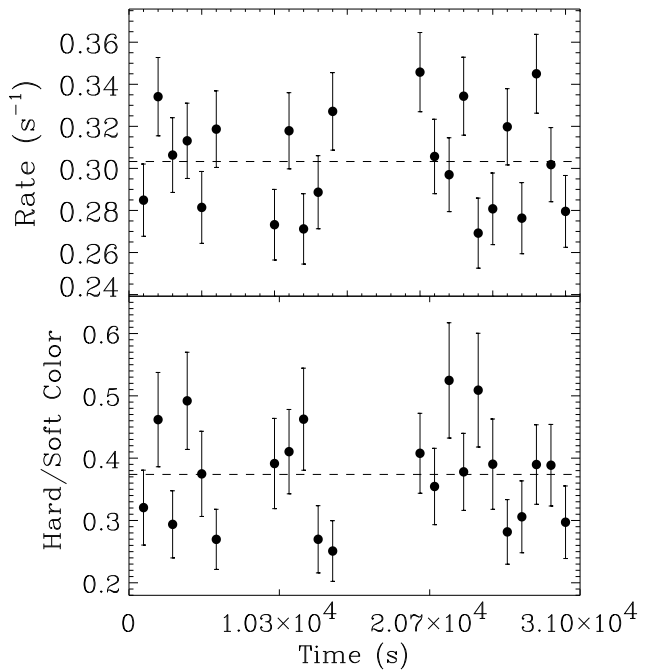


Fig. 3. EPIC pn light curves of the background-subtracted count rate in the 0.3–10 keV band (top panel) and of the X-ray color 2–10 keV/0.3–0.8 keV (bottom panel). The extraction radius is 20''; time bins are 1000 s. The dashed lines indicate the average values.

a consequence, they suffer from low photon statistics and their intensity variations are basically statistical fluctuations randomly distributed. Thus the net effect of adding the MOS light curves to the pn one results in an overall decrease of the level of variability. In the following, therefore, we will use data only from the pn camera (0.3–10 keV). To examine the influence of the extraction radius on the variability we extracted pn light curves from circular regions of radii ranging between 10'' and 30''. According to a χ^2 test, the flux variability is most pronounced when the extraction radius is 20''. This choice represents a compromise between the necessity to increase the photon statistics

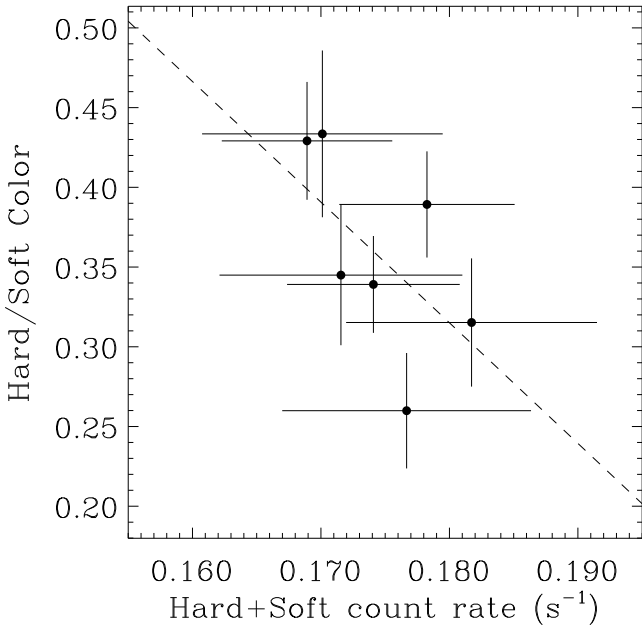


Fig. 4. EPIC pn X-ray color (2–10 keV/0.3–0.8 keV) versus the count rate (2–10 keV + 0.3–0.8 keV); time bins are 4000 s. The dashed line indicates the result of a linear least square fit, showing a marginally significant ($P_c(r) = 7.5\%$) anti-correlation.

and to minimize the contribution of the extended emission, which is particularly important at soft energies (see Figure 1). We then extracted energy-selected light curves in the ultra-soft (0.3–0.8 keV), soft (0.8–2 keV), and hard (2–10 keV) energy bands. In Table 2 we summarize the results of the short-term variability analysis obtained using time bins of 1000 s.

Figure 3 shows the background-subtracted light curve from the EPIC pn in the total energy range 0.3–10 keV (top panel). The bottom panel shows a plot of the hardness ratio, defined as the ratio of the 2–10 keV count rate to the 0.3–0.8 keV count rate, versus time. Low-amplitude variations are present in both cases, confirming our previous results (Paper I). Applying a χ^2 test against the hypothesis of constancy, we find that variability is highly significant in both light curves: χ^2 probabilities of 0.6% and 3% are found for the flux and hardness ratio, respectively. The background count rate is as low as 5% of the average source count rate and, after removing two large flares, is consistent with the hypothesis of being constant, according to a χ^2 test. To investigate the presence of possible systematic effects in the variability analysis, we extracted light curves from the only additional point-like source located on CCD4, and from two of the brightest serendipitous sources located in the EPIC f.o.v. far from CCD edges (RA=12^h19^m50.1^s, DEC=+05°51′04.75″, RA=12^h19^m21.5^s, DEC=+05°42′02.73″, and RA=12^h19^m04.7^s, DEC=+05°49′04.8″, respectively). All the sources are ~ 3 times fainter than the central source,

and none of them is significantly variable according to χ^2 testing.

The variability in different energy bands can be characterized by means of the fractional variability parameter, F_{var} . The latter is a common measure of the intrinsic variability amplitude relative to the mean count rate, corrected for the effect of random errors, i.e.,

$$F_{\text{var}} = \frac{(\sigma^2 - \Delta^2)^{1/2}}{\langle r \rangle}, \quad (3)$$

where σ^2 is the variance, $\langle r \rangle$ the unweighted mean count rate, and Δ^2 the mean square value of the uncertainties associated with each individual count rate. Using different binning times ranging between 200 s and 1000 s, we calculated F_{var} in the 0.3–0.8 keV band and in the 2–10 keV band. For any binning time, $F_{\text{var-ultrasoft}}$ is larger than $F_{\text{var-hard}}$. For example, $F_{\text{var-ultrasoft}} \sim 10 \times 10^{-2}$ for 200 s and $\sim 9 \times 10^{-2}$ for 1000 s, respectively, while $F_{\text{var-hard}} \sim 5.5 \times 10^{-2}$ for 200 s and $\sim 7 \times 10^{-2}$ for 1000 s bins.

Spectral variations are also present, as shown in Figure 3. An interesting trend may be present when the hardness ratio is plotted versus the total count rate. This is illustrated in Figure 4, which shows the presence of a marginally significant anti-correlation between the hardness ratios and the total intensity. To quantify the degree of linear correlation between $Hard/Soft$ and the mean count rate, we calculated the linear correlation coefficient $r = -0.62$ and computed the chance probability that a random sample of uncorrelated pairs of measurements would yield a linear correlation coefficient equal or larger than $|r|$, finding $P_c(r) = 7.5\%$.

5. Spectral Analysis

5.1. The X-ray continuum

In Paper I, we presented an analysis of the EPIC pn spectrum from 0.3–10 keV. It was best-fit by a model consisting of a thermal component related to the diffuse halo, dominating from 0.6–2 keV; a heavily absorbed power law above 2 keV, of nuclear origin; and a second unabsorbed power law dominating the ultra-soft 0.3–0.8 keV emission, with the photon index tied to that of the hard power law. The two power-law model mimics a partial-covering model. This represents the physical situation of an absorber only partially covering the nucleus, with the softer power law representing the fraction of the flux which “leaks through” the patchy medium (e.g., Holt et al. 1980). We therefore investigated the combined spectra from the pn, MOS1, and MOS2 cameras (after checking the consistency of each spectrum individually) using a thermal model plus a partially absorbed power law. Specifically, we fitted the *XMM-Newton* EPIC data from 0.3–10 keV with the following model: a thermal component, parameterized by `appec` in `XSPEC`, plus a partially absorbed power law, parameterized by `zpcfabs(powerlaw)`, plus a uniform screen of absorbing gas with its column

Table 3. Spectral properties of NGC 4261 as seen by the *XMM-Newton* EPIC cameras and the *Chandra* ACIS-S3.

Parameter	<i>XMM-Newton</i>	<i>Chandra</i>
kT (keV)	$0.65^{+0.01}_{-0.02}$	$0.60^{+0.02}_{-0.02}$
Z (Z_{\odot})	1 (> 0.4)	1
N_{H} (10^{22} cm^{-2})	$5.1^{+1.1}_{-1.2}$	$6.8^{+2.5}_{-2.1}$
CvrFract	$0.81^{+0.06}_{-0.09}$	$0.90^{+0.06}_{-0.07}$
Γ	$1.46^{+0.17}_{-0.31}$	$1.14^{+0.43}_{-0.38}$
E_{line} (keV)	$6.99^{+0.08}_{-0.09}$	
σ (keV)	$0.03^{+0.15}_{-0.03}$	
EW (eV)	230^{+166}_{-134}	
line flux ($10^{-6} \text{ s}^{-1} \text{ cm}^{-2}$)	$1.7^{+1.3}_{-1.0}$	
$\chi^2/d.o.f.$	400.91/359	76.15/71
Counts	11708	222
$L_{0.3-2 \text{ keV}}$ ($10^{40} \text{ erg s}^{-1}$)	8.6	3.6
$L_{2-10 \text{ keV}}$ ($10^{40} \text{ erg s}^{-1}$)	8.3	9.5

density fixed to the Galactic value ($1.52 \times 10^{20} \text{ cm}^{-2}$), acting on all components. The data with the best-fit model and the residuals are shown in Figure 5 (top panel), while the best-fit parameters with their 90% uncertainties are listed in Table 5. Line-like residuals are present at ~ 4.8 keV; however, adding a Gaussian line at that energy does not improve the fit significantly. The 0.3–10 keV unabsorbed flux associated with the thermal component is $F_{\text{X,apcc}} = 4.6 \times 10^{-13} \text{ erg cm}^{-2} \text{ s}^{-1}$, whereas the flux associated with the power-law component is $F_{\text{X,pow}} = 11.2 \times 10^{-13} \text{ erg cm}^{-2} \text{ s}^{-1}$. We find that the same continuum model fits the *Chandra* ACIS-S data from 0.3–9 keV. The results of this spectral fit along with the intrinsic luminosities are also listed in Table 5, for direct comparison with *XMM-Newton*, and the residuals are shown in Figure 5 (middle panel).

The *XMM-Newton* and *Chandra* best-fit parameters are consistent within the 90% errors, with the exception of the temperature of the diffuse halo, which is slightly lower in the *Chandra* spectral fit. This is likely due to a shallow temperature gradient in the circumnuclear region very close to the central source. Indeed, dividing the inner $30''$ into six annular regions and comparing the spatially-resolved *Chandra* spectra, we find a shallow temperature gradient with kT going from 0.6 to 0.8 keV but with large uncertainties due to the limited statistics. The larger 0.3–2 keV luminosity measured by *XMM-Newton* can be ascribed to the larger extraction area ($20''$ vs. $2''$) used, meaning a stronger contribution from the thermal component that actually peaks in the soft X-ray range.

The *Chandra* data were previously analyzed by Chiaberge et al. (2003). These authors found that a single absorbed power law plus a thermal plasma best-fits the S3 data ($\chi^2/dof = 90/69$). The different spectral results can be partially ascribed to the different processing

of the data: 1) we use the latest released calibration files (CALDB v2.18); 2) we apply ACISABS to the ARF file to account for the degradation of the QE due to molecular contamination; 3) we did not convolve our spectral model with `pileup` in XSPEC, because, according to a test with PIMMS, the pile-up in NGC 4261 is less than 5%. In any case, from the statistical point of view our fit is significantly better than that of Chiaberge et al. (2003).

We also tried to fit the data with more complex spectral models, e.g., `pexrav` or the ionized-disk reflection model of Ross & Fabian (1993). However, the fit did not improve.

The spectral analysis of the *BeppoSAX* data is inconclusive. The spectrum fitted by a thermal component ($kT = 0.65 \pm 0.3$ keV) plus an absorbed power law ($N_{\text{H}} \sim 7 \times 10^{21} \text{ cm}^{-2}$, $\Gamma = 1.3 \pm 0.3$) gives a reduced χ^2 of ~ 0.5 for 49 d.o.f. Similar results are obtained using more complex spectral models. The low value of χ^2_{red} indicates that the fit is dominated by the large statistical errors due to the poor photon statistics. However, it is important to point out that the PDS detected the source up to energies higher than 100 keV at more than a 3σ confidence level. The flux is $\sim 6 \times 10^{-12} \text{ erg cm}^{-2} \text{ s}^{-1}$ in the 10–100 keV range, implying an intrinsic luminosity of $\sim 6.5 \times 10^{41} \text{ erg s}^{-1}$.

5.2. The Fe line

Another important result of Paper I was the detection of an unresolved Fe K line at ~ 7 keV in the EPIC pn data. Unfortunately, due to their limited sensitivity, the MOS data do not provide any constraint on the Fe K line (Fig. 5). In Figure 6, we show the contours at 68%, 90%, 95%, and 99% confidence level from the EPIC pn data for the line flux versus width. It is apparent that the line is detected at $\gtrsim 95\%$ confidence and is not significantly resolved. A broad line cannot be excluded. As mentioned in Paper I, no Fe line is detected in the *Chandra* ACIS S3 data, with an EW upper limit of 320 eV. On the other hand, the *BeppoSAX* MECS data show evidence for the Fe line, as indicated by the excess in the residuals around 6–8 keV (see Fig. 5, bottom panel). Adding a Gaussian model with the width fixed at the best-fit value from the EPIC pn data to the best-fit MECS continuum gives a slight improvement in the fit ($\Delta\chi^2 = 2.4$ for two additional parameters). The line parameters are consistent with those from the EPIC pn, $E = 6.7 \pm 0.7$ keV, $EW = 304^{+460}_{-304}$ eV. Thus, we confirm the previous claim based on a 40 ks *ASCA* exposure that an Fe line is present in the spectrum of NGC 4261 (Terashima et al. 2002; Sambruna et al. 1999). The line energy is consistent with emission from Fe XXVI. However, as discussed in Paper I, the origin of the line and the nature of the reprocessor are still unclear. A deeper exposure with the EPIC pn is necessary to study the line profile in more detail.

6. Discussion

6.1. Summary of X-ray Results

We first summarize the main observational results that will be relevant for the discussion of the nuclear properties of NGC 4261.

From the deprojected density profile (Eq. 2) and the spectral analysis of the diffuse halo, one can place an upper limit on the accretion rate from the interstellar medium onto the central black hole by applying the Bondi theory of spherical accretion (Bondi 1952). Specifically, the Bondi accretion rate can be written (see, e.g., Di Matteo et al. 2003)

$$\dot{M}_{\text{Bondi}} = 4\pi R_A^2 \rho_A c_s, \quad (4)$$

where $R_A \simeq GM/c_s^2$ is the accretion radius, $c_s \sim 10^4 T^{1/2} \text{ cm s}^{-1}$ the sound speed, and ρ_A the density at the accretion radius. According to the above definition of R_A and using the best-fit gas temperature, $kT \simeq 0.60 \text{ keV}$ (see §5), the accretion radius of NGC 4261 is located at $\sim 0.4'' \simeq 55 \text{ pc}$. Extrapolating the density profile to this distance, we derive $\dot{M}_{\text{Bondi}} \simeq 0.04 M_\odot \text{ yr}^{-1}$. This value can be used to calculate the expected accretion luminosity. Assuming a canonical radiative efficiency of 10%, we find $L_{\text{accr}} \sim 2.5 \times 10^{44} \text{ erg s}^{-1}$.

From the best-fit spectral model, after correcting for the covering fraction and the local absorption, the 0.3–10 keV luminosity associated with the nuclear non-thermal component is $L_{\text{non-therm}} \sim 1.2 \times 10^{41} \text{ erg s}^{-1}$. The estimate of the X-ray luminosity can be further increased to $\sim 7 \times 10^{41} \text{ erg s}^{-1}$ by extending the spectrum up to 100 keV, as observed with the PDS aboard *BeppoSAX*. It is worth noticing that the non-thermal luminosity is ~ 350 times smaller than the accretion luminosity inferred assuming $\dot{M}_{\text{accr}} = \dot{M}_{\text{Bondi}}$.

The main results of the timing analysis are 1) the presence of rapid variability on time scales of a few ks; 2) the fact that the variability is more pronounced in the ultra-soft 0.3–0.8 keV energy band than in the hard 2–10 keV energy band; and 3) the possible existence of an anti-correlation between the hardness ratio and the total count rate.

6.2. Properties of the VLBI Jet

One of the goals of this paper is to determine the extent to which the jet contributes to the nuclear X-ray emission from NGC 4261. In this section, we investigate the properties of the pc-scale jet focusing on its energetic requirements.

It is generally believed that the most important power content of extragalactic jets is not in the form of internal random energy giving rise to observed radiation, but in the form of kinetic power associated with particles and magnetic fields. This requirement comes from the power budget of extended radio structures, which need an average supply greater than the luminosity generated by the

jet at all scales (e.g., Rawlings & Saunders 1991; Ghisellini & Celotti 2001).

The total power transported by the flow is thus a fundamental property for the discussion of jet energetics. An estimate of the *minimum* jet kinetic power can be obtained following the method of Gliozzi, Bodo & Ghisellini (1999). This method assumes that the energy flux flowing through the cross-section of the jet is carried by particles, $L_{\text{k,part}} = \pi R^2 \Gamma^2 \beta c n' (\langle \gamma \rangle m_e + m_+) c^2$, and magnetic fields, $L_{\text{k,B}} = \pi R^2 \Gamma^2 \beta c U_B$, where R is the radius of the jet cross-section, Γ the bulk Lorentz factor, $\beta = v/c$, n' the comoving particle density, $\langle \gamma \rangle$ the mean Lorentz factor of the electrons, and U_B the magnetic energy density. The quantity m_+ is either the proton mass m_p in the case of “normal” plasma, or the positron mass $\langle \gamma \rangle m_{e^+}$ for e^\pm pairs. A lower limit on the electron density n' can be estimated from the observed synchrotron emission L_{syn} . Approximating the VLBA jet as a cylinder of radius R and length h , the number density of leptons producing the observed radiation is $n = 6L_{\text{syn}} / (\langle \gamma^2 \rangle \delta^4 \sigma_T c B^2 h R^2)$, where $\langle \gamma^2 \rangle$ is averaged over the relativistic electron distribution, $\delta = [\Gamma(1 - \beta \cos \theta)]^{-1}$ is the Doppler factor, and σ_T is the Thomson cross-section. As the kinetic power associated with the particles has a dependence on the magnetic field, $L_{\text{k,part}} \propto B^{-2}$, the total kinetic power can be minimized with respect to the magnetic field, $\partial L_{\text{k,tot}} / \partial B = 0$. This yields a value of the magnetic field B_{min} corresponding to the minimum power.

In blazars, where jets on pc-scales are unresolved due to the small viewing angle, the jet parameters have to be inferred indirectly by modelling the spectral energy distributions (SED) with specific models (e.g., Tavecchio et al. 2000). On the other hand, in the case of NGC 4261 the pc-scale jet parameters are obtained directly from VLBA observations (Jones & Wehrle 1997; Piner, Jones, & Wehrle 2001). The jet spectral index is $\alpha = 0.29 \pm 0.07$ ($f \propto \nu^{-\alpha}$), and therefore the index of the electron energy distribution is $p = 2\alpha + 1 = 1.58$. The jet velocity and inclination to the line of sight are $\beta = 0.46$ and $\theta = 63^\circ$, respectively; as a consequence the bulk Lorentz factor is $\Gamma = 1.126$ and the Doppler factor is $\delta = 1.122$. The synchrotron luminosity derived from radio data is $L_{\text{syn}} \simeq 3 \times 10^{39} \text{ erg s}^{-1}$. Note that a possible contribution from the UV jet is less than 10% of the radio luminosity (Chiaberge et al. 2003). A negligible contribution to the synchrotron luminosity is expected from the X-rays on a twofold basis: 1) the steepness of the electron energy distribution, and 2) the fact that the SED of NGC 4261 has a secondary broad peak located in the X-ray range (Lewis et al. 2003). From the VLBA images the jet has transverse and longitudinal dimensions of $\sim 2 \text{ mas}$ and $\sim 14 \text{ mas}$, which correspond to $R \simeq 8.8 \times 10^{17} \text{ cm}$ and $h \simeq 6.9 \times 10^{18} \text{ cm}$ after deprojecting the longitudinal dimension.

The main uncertainties in deriving the jet kinetic luminosity are the low- and high-energy cutoffs in the electron energy distribution, γ_{min} and γ_{max} , respectively. An upper limit $\gamma_{\text{max}} \lesssim 4 \times 10^5$ can be determined assuming that the radio-to-UV emission is due to synchrotron emission

from the same electron population. This is a reasonable assumption for a mildly relativistic jet, as inferred from the VLBA observations of NGC 4261 (see Chiaberge et al. 2003 for a detailed discussion of the UV jet). Given the steep electron energy distribution, most of the energy is stored in low-energy electrons, and therefore the low-energy cutoff plays a more important role than γ_{\max} . Since there is no direct and secure way to set a lower limit on γ_{\min} , we carried out the calculation of L_{kin} assuming γ_{\min} ranging between 1 and 30 (typical values inferred by blazar SED modelling; e.g., Tavecchio et al. 2000), and we evaluated the influence of the low-energy cutoff on B_{\min} and $L_{\text{kin},\min}$.

The magnetic field corresponding to the minimum power is $B_{\min} = 3.3$ mG, for a “normal” plasma and $\gamma_{\min} = 1$. A somewhat lower value, $B_{\min} = 2.4$ mG, is found assuming $\gamma_{\min} = 30$. Similar values are found in the case of pair plasma: $B_{\min} \simeq 2.5$ mG. With a magnetic field strength equal to B_{\min} , the particle kinetic power and the Poynting flux are nearly equal, and the total power $L_{\text{k,tot}}$ ranges between 3.7×10^{40} erg s $^{-1}$ and 1×10^{40} erg s $^{-1}$ for normal and pair plasmas, respectively. Slightly lower values are found assuming a low energy cut-off of 30.

The jet kinetic power must be multiplied by two to take into account the contribution from the counter-jet. It is worth noticing that while the values of B_{\min} are of the same order as the ones derived for blazars, the kinetic luminosity is significantly lower. This is due to the low value of Γ inferred from the VLBA observations; assuming $\Gamma = 10$, as in blazars, the kinetic luminosity increases by several orders of magnitude ($L_{\text{k,tot}} \sim 2 \times 10^{44}$ erg s $^{-1}$) and becomes consistent with the values typically inferred for BL Lacs.

6.3. Origin of the nuclear X-ray emission

The strong correlation between radio and X-ray core fluxes found in low-luminosity (Fabbiano et al. 1984; Canosa et al. 1999) and high-luminosity (Worrall et al. 1994; Hardcastle et al. 1998) radio galaxies has often been used to argue in favor of a common origin from the unresolved base of the jet for the emission at the two wavelengths (e.g., Hardcastle & Worrall 1999 and references therein). More recently, a jet origin for the X-rays was claimed for several low-power radio galaxies observed with *Chandra* (Pellegrini et al. 2003; Fabbiano et al. 2003; Chiaberge et al. 2003).

We note the following:

1) While the strong correlation between radio and X-ray fluxes does suggest a physical connection, it does not necessarily imply a common jet origin of the two fluxes. Indeed, accretion onto compact objects and relativistic jets seem to be correlated phenomena (e.g. Begelman, Blandford & Rees 1984). As a consequence, at some level,

a correlation between the jet and the disk-corona² flux is expected.

2) The claim of a jet origin for the X-rays, in addition to the radio-X-ray correlation, is based on spectral results. However, a common problem affecting the study of AGN is spectral degeneracy: the same spectrum can be equally well described by quite different spectral models. This is exacerbated in the case of low-power radio galaxies, due to their low signal-to-noise ratio X-ray spectra. For example, in the case of NGC 4261, the photon index $\Gamma \sim 1.5 \pm 0.3$ is consistent with inverse Compton emission from a jet but also with an advection dominated accretion flow (ADAF) model. It is worth noticing that Fabbiano et al. (2003) fit satisfactorily the radio-to-X-ray SED of the low-luminosity radio galaxy IC 1459 with a jet-dominated model. However, as already highlighted by Di Matteo et al. (2001a) for several nearby galaxies, this simply indicates that analytical ADAF models are unable to account for the high radio flux and that an additional contribution, possibly from a small-scale radio jet, is required. It does not necessarily imply that a pure jet model is the solution. In fact, this latter model, tentatively applied to higher quality and much broader bandpass energy spectra, is far from being widely accepted yet (e.g., Zdziarski et al. 2003).

In order to break the spectral degeneracy, one needs to exploit additional information coming, for example, from temporal analysis. Relying upon timing and spectral variability results from long monitoring campaigns of two powerful broad-line radio galaxies (BLRG; 3C 390.3 and 3C 120), Gliozzi, Sambruna & Eracleous (2003) concluded that the X-ray emission is not dominated by jets. Both BLRGs display typical X-ray behavior observed in Seyfert galaxies, namely a softer X-ray spectrum with increasing flux (e.g., Petrucci et al. 2000; Vaughan & Edelson 2001; Papadakis et al. 2002) and a larger variability amplitude in soft X-rays (Nandra et al. 1997; Markowitz & Edelson 2001). Moreover, jet-dominated sources, i.e., blazars, typically show the opposite temporal and spectral behavior: the X-ray spectrum hardens when the flux increases and the variability amplitude increases toward higher energies (see, e.g., Zhang et al. 1999; Fossati et al. 2000). In the case of NGC 4261, the temporal and spectral variability behavior similar to that shown by 3C 390.3 and 3C 120 (although with a lower statistical significance) is suggestive evidence that most of the X-rays originate from the disk-corona system. This favors the conclusion that the jet is not the dominant mechanism producing the X-rays in the nucleus of NGC 4261.

This conclusion is independently confirmed if we compare the jet kinetic power with the X-ray luminosity. Let us assume that most of the X-rays originate from the jet; this would lead to the unphysical conclusion that the radiative power of the jet is more important than its kinetic power. This would be at odds with the energetic re-

² For simplicity, we use the term “disk corona” to indicate any type of accretion flow at work around the black hole.

quirements of the lobes (see §6.2). One can object that the estimated L_{kin} represents only the minimum value for the kinetic power of the jet, and that, if the jet is not in equipartition, this value can significantly increase. However, one must keep in mind that 1) moderate departures from equipartition do not increase L_{kin} by orders of magnitude (Ghisellini & Celotti 2001); 2) typical values for the kinetic-to-radiative luminosity ratio in radio-loud AGNs are estimated to be $\sim 10^2 - 10^4$ (see, e.g., Celotti & Fabian 1993).

6.4. Nature of the accretion flow

Before starting the discussion on the nature of the accretion flow, it is necessary to emphasize the distinction between radiatively inefficient accretion flow (RIAF) and ADAF models. The former class describes the properties of rotating accretion flows where very little of the accretion energy is radiated away, whereas ADAF models are simple analytical models for the dynamics of RIAF models. The most relevant difference is that ADAF models predict that the rate at which gas accretes onto the black hole is comparable to the Bondi accretion rate; therefore, the low luminosity in ADAF models is just due to very low radiative efficiency. On the other hand, time-dependent numerical simulations of RIAF models indicate that $\dot{M}_{\text{accr}} \ll \dot{M}_{\text{Bondi}}$, implying that the observed low luminosity is also due to a low accretion rate, rather than just a low efficiency. For a more detailed discussion of RIAF models see, e.g., Quataert (2003).

Recently, *Chandra* studies of the nature of the accretion flows in several giant elliptical galaxies have returned some controversial results on the relation between \dot{M}_{Bondi} and \dot{M}_{accr} . For example, Di Matteo et al. (2001b, 2003) question whether \dot{M}_{Bondi} is a reliable estimate of \dot{M}_{accr} and whether the ADAF model is a viable solution for NGC 6166 and M87. In this latter case, if feedback effects from the base of the jet on the accretion flow are taken into account, \dot{M}_{accr} can be as low as $10^{-6}\dot{M}_{\text{Bondi}}$. Also Loewenstein et al. (2001) conclude that \dot{M}_{accr} must be significantly smaller than \dot{M}_{Bondi} to find X-ray fluxes in agreement with the values observed by *Chandra* for NGC 1399, NGC 4472, and NGC 4636. On the other hand, Pellegrini et al. (2003) and Fabbiano et al. (2003), investigating respectively IC 4296 and IC 1459, conclude that \dot{M}_{Bondi} can be a reliable estimate of \dot{M}_{accr} . However, the authors exclude the ADAF scenario on the basis of SED considerations, in particular the high radio-to-X-ray flux ratio, favoring instead a jet-dominated model.

In the case of NGC 4261, on the basis of the *Chandra* data alone and according to the Bondi theory, the first conclusion is that the black hole is not fuel-starved ($\dot{M}_{\text{Bondi}} \sim 0.04 M_{\odot} \text{ yr}^{-1}$). Given that the expected accretion luminosity $L_{\text{accr}} \sim 2.5 \times 10^{44} \text{ erg s}^{-1}$ (assuming a canonical efficiency of 10%) is much higher than the disk-corona luminosity, we would be tempted to conclude that accretion is radiatively inefficient. Indeed, using the results

derived by Loewenstein et al. (2001) for NGC 1399 (which has M_{BH} and M_{Bondi} similar to those of NGC 4261), by applying the basic ADAF model, we can conclude that the 2–10 keV luminosity of NGC 4261 is roughly consistent with L_{ADAF} . Therefore, disregarding the problem of the high radio-to-X-ray flux ratio, possibly solved by ascribing to the base of the jet most of the core radio emission (see e.g., Di Matteo et al. 2001a), at the zeroth order an ADAF (+ radio jet) seems to be an acceptable solution.

An independent way to test whether \dot{M}_{Bondi} is a reliable estimate of \dot{M}_{accr} is based on a comparison between the accretion rate and outflow rate, \dot{M}_{out} , which can be derived from the kinetic energy of the jet: $L_{\text{k}} = (\Gamma - 1)\dot{M}_{\text{out}}c^2$. Assuming $\dot{M}_{\text{Bondi}} = \dot{M}_{\text{accr}}$ and the value of the kinetic power derived in §6.2, the conclusion would be that $\dot{M}_{\text{out}} \sim 10^{-4}\dot{M}_{\text{accr}}$. This value seems low considering that studies of the jet-disk luminosities of the BL Lac class (the parent population of FR I according to the unification models; e.g., Urry & Padovani 1997) indicate that the channelling of matter from the accretion flow into the jet outflow seems to be particularly efficient. For example, Maraschi & Tavecchio (2003) find that for BL Lacs $L_{\text{disk}}/L_{\text{k}} \sim 10^{-3} - 10^{-4}$. Applying this result to NGC 4261 with $L_{\text{disk}} = \eta\dot{M}_{\text{accr}}c^2$, $M_{\text{accr}} = M_{\text{Bondi}}$, and L_{k} given by the above formula, we obtain an unphysically low radiative efficiency, $\eta \sim 10^{-8} - 10^{-9}$.

Further independent evidence that the $\dot{M}_{\text{out}}/\dot{M}_{\text{accr}}$ derived for NGC 4261 is unreasonably small comes from MHD simulations that show that most of the inflowing flow is lost in a magnetically driven wind (e.g., Stone & Pringle 2001; Hawley & Balbus 2002). As a consequence, energetic considerations favor a RIAF model, where the intrinsically low luminosity of NGC 4261 is explained in terms of low accretion rate coupled with a moderately low radiative efficiency.

Additional important pieces of information can come from the *XMM-Newton* observations, in particular from the temporal analysis. Even though, historically, rapid X-ray variability in AGN has been associated with standard accretion disks, ADAF models can also account for such variability if the X-rays are produced by Compton process in the inner region of the accretion flow. The rapid flux variations detected from NGC 4261 indicate that such variability can actually occur also in low-power AGNs and that RIAF models should account for this temporal behavior consistently. Indeed, the rapid X-ray flares observed from Sgr A* have been recently interpreted by Yuan et al. (2003) in the framework of radiatively inefficient accretion flow models.

7. Summary and Conclusions

We have presented *XMM-Newton*, *Chandra*, and *BeppoSAX* observations of the low-power FR I radio galaxy NGC 4261, host of a supermassive black hole and an optical LINER. The main findings can be summarized as follows:

- Several spatial components are present in the X-ray

image: an unresolved nuclear region, present in all energy bands; a diffuse hot halo, dominating the 0.6–2 keV emission; a double-sided kpc-scale jet; and several point-like sources. The jet and the point sources give a negligible contribution to the X-ray flux in the *XMM-Newton* aperture.

- The surface brightness of the extended circumnuclear emission is well fitted with a β -model ($\beta \simeq 0.53$, $r_c \simeq 1.40''$). Combining these results with the spectral analysis ($kT \sim 0.6 - 0.65$ keV) and using the Bondi theory, an accretion rate of $\dot{M} \simeq 0.04 M_{\odot} \text{ yr}^{-1}$ is found, corresponding to an accretion luminosity of $L_{\text{accr}} \sim 2.5 \times 10^{44} \text{ erg s}^{-1}$ for a radiative efficiency of 10%.

- The spectrum of the nucleus is well described from 0.3–10 keV by a power law with $\Gamma \simeq 1.5$, partially covered by cold gas ($\text{CvrFract} \simeq 0.8$, $N_{\text{H}} \simeq 5 \times 10^{22} \text{ cm}^{-2}$), plus a highly ionized unresolved iron line at ~ 7 keV. The presence of a line is confirmed by *BeppoSAX*, which also detects at the 3σ level high-energy emission up to 100–150 keV.

- The total non-thermal luminosity in the 0.3–10 keV band is $1.2 \times 10^{41} \text{ erg s}^{-1}$ ($\sim 7 \times 10^{41} \text{ erg s}^{-1}$ between 0.3 and 100 keV), which is more than 2 orders of magnitude lower than the expected accretion luminosity.

- Significant flux and spectral variations of the nuclear X-ray emission were detected with EPIC. The variability is more pronounced in the soft band (0.3–0.8 keV), and the hardness ratio appears to be anti-correlated with the count rate. We conclude that most of the nuclear X-ray emission is related to the accretion flow and that the base of the jet is *not* the dominant source of X-rays from the nucleus of NGC 4261.

- Energetic arguments based on the jet kinetic power support this conclusion and suggest that the Bondi accretion rate overestimates (presumably by orders of magnitude) the actual accretion rate onto the black hole. Therefore, the low X-ray luminosity of NGC 4261 can be explained in terms of low accretion rate coupled with a moderately low radiative efficiency, not just a very low efficiency as hypothesized by ADAF models. These results suggest some general conclusions. Although great progress in the study of accretion in AGN is made by comparing spectral models with the data, spectral results alone cannot unequivocally constrain the origin of the X-rays and the nature of the accretion onto the central black hole. This is especially true for low-power radio galaxies, whose low signal-to-noise spectra can be acceptably fitted with completely different physical models. Spectral analysis is further complicated by the presence of several distinct components contributing to the total X-ray emission. Major progress in the understanding of accretion phenomena can only be reached by combining spectral results with independent information from spatial and timing analyses. To this aim, constraints from *both Chandra* and *XMM-Newton* are needed.

APPENDIX

Serendipitous sources in the Chandra field

The *Chandra* ACIS-S image of NGC 4261 in the 0.3–10 keV energy range (Figure 1, bottom right panel) reveals the presence of several off-nuclear point sources. We used the CIAO tool *wavdetect* to search for serendipitous X-ray sources in the f.o.v. The algorithm returns a list of ellip-

Table 4. Off-nuclear X-ray point-like sources

Source	RA (J2000)	DEC (J2000)	Counts ^a [0.35–9 keV]	D ^b [']
A	12 ^h 19 ^m 24.9 ^s	+05°49'32''	15 ± 4	26
B	12 ^h 19 ^m 24.0 ^s	+05°49'27''	33 ± 7	13
C	12 ^h 19 ^m 23.5 ^s	+05°49'36''	81 ± 10	7.5
D	12 ^h 19 ^m 22.7 ^s	+05°49'43''	22 ± 5	15.5
E	12 ^h 19 ^m 20.3 ^s	+05°49'27''	15 ± 4	34

^a For comparison, the number of counts found in the central 2'' source region is 2254 ± 47 .

^b Distance in arcsecond from NGC 4261.

tical regions that define the positions and the shapes of the detected sources (see Table 4). We next used the coordinates from *wavdetect* and its associated error regions to search for optical counterparts on ESO archival plates and *HST* images. However, none of the five serendipitous sources has an apparent optical counterpart. Source *C* has enough counts for temporal and spectral analyses. The spectrum, which extends only in the 0.5–1.5 keV range, is well fitted by a simple power law ($\Gamma = 2.3 \pm 0.6$) absorbed by Galactic $N_{\text{H}} = 1.52 \times 10^{20} \text{ cm}^{-2}$, with an absorbed flux of $f_{0.5-1.5\text{keV}} = 8 \times 10^{-15} \text{ erg cm}^{-2} \text{ s}^{-1}$. The light curve is consistent with the source flux being constant ($P_{\chi^2} > 99.9\%$).

Acknowledgements. We are grateful to T. Cheung, M. Chiaberge, T. Di Matteo, D. Donato, M. Eracleous, J. Krolik, Alex Rinn, and F. Tavecchio for helpful discussions. Financial support from NASA LTSA grants NAG5-10708 (MG, RMS) and NAG5-13035 (WNB) is gratefully acknowledged. Funds were also provided by NASA grant NAG5-10243 (MG, RMS) and by the Clare Boothe Luce Program of the Henry Luce Foundation (RMS).

References

- Arnaud, K. 1996, in ASP Conf. Ser. 101, *Astronomical Data Analysis Software and Systems V*, ed. G. Jacoby & J. Barnes (San Francisco: ASP), 17
- Begelman, M.C., Blandford, R.D., & Rees, M.J. 1984, *Rev. Mod. Phys.*, 56, 255
- Binney, J., & Tabor, G. 1995, *MNRAS*, 276, 663
- Bondi, H. 1952, *MNRAS*, 112, 195

- Canosa, C.M., Worrall, D.M., Hardcastle, M.J., & Birkinshaw, M. 1999, MNRAS, 310, 30
- Cavaliere, A., & Fusco-Femiano, R. 1976, A&A, 49, 137
- Celotti, A., & Fabian, A.C. 1993, MNRAS, 264, 228
- Chiaberge, M., Gilli, R., Macchetto, F.D., Sparks, W.B., & Capetti, A. 2003, ApJ, 582, 645
- Ciotti, L., & Ostriker, J.P. 2001, ApJ, 551, 131
- Di Matteo, T., Carilli, C.L., & Fabian, A.C. 2001a, ApJ, 547, 731
- Di Matteo, T., Johnstone, R.M., Allen, S.W., & Fabian, A.C. 2001b, ApJ, 550, L19
- Di Matteo, T., Allen, S.W., Fabian, A.C., Wilson, A.S., & Young, A.J. 2003, ApJ, 582, 133
- Donato, D., Gliozzi, M., Sambruna, R.M., & Pesce, J.E. 2003 A&A, in press (astro-ph/0305407)
- Edelson, R., Turner, T.J., & Pounds, K. 2002, ApJ, 568, 610
- Ettori, S. 2000, MNRAS, 311, 313
- Fabbiano, G., Miller, L., Trinchieri, G., Longair, M., & Elvis, M. 1984, ApJ 277, 115
- Fabbiano, G., Elvis, M., Markoff, S., et al., 2003, ApJ in press (astro-ph/0301297)
- Ferrarese, L., Ford, H.C., & Jaffe, W. 1996, ApJ, 470, 444
- Ferrarese, L., Pogge, R.W., Peterson, B.M., et al. 2001, ApJ, 555, L79
- Fiore F., Guainazzi M., Grandi P., 1999, Handbook for BeppoSAX NFI spectral analysis
- Forman, W., Jones, C., & Tucker, W. 1985, ApJ, 293, 102
- Fossati, G., Celotti, A., Chiaberge, M., et al., 2000, ApJ, 541, 153
- Gebhardt, K., Kormendy, J., Ho, L.C., et al. 2000, ApJ, 543, L5
- Ghisellini, G., & Celotti, A. 2001, MNRAS, 327, 739
- Gliozzi, M., Bodo, G., & Ghisellini, G. 1999, MNRAS, 303, L37
- Gliozzi, M., Sambruna, R.M., & Eracleous, M. 2003, ApJ, 584, 176
- Hardcastle, M.J., Lawrence, & C.R. Worrall, D. M. 1998, ApJ, 504, 743
- Hardcastle, M.J., & C.R. Worrall, D. M. 1999, MNRAS, 309, 969
- Hawley, J.F., & Balbus, S.A., 2002, ApJ, 573, 738
- Heckman T.M., 1980, A&A, 87, 152
- Ho, L. C., Filippenko, A. V., & Sargent, W. L. W. 1995, ApJS, 98, 477
- Holt, S.S., Mushotzky, R.F., Boldt, E.A., et al. 1980 ApJ, 241, 13L
- Jones, D.L., & Wehrle, A.E. 1997, ApJ, 484, 186
- Lawrence, A. 1999, AdSpR, 23, 1167
- Lewis, K.T., Eracleous, M., & Sambruna, R.M. 2003 ApJ in press (astro-ph 0304399)
- Loewenstein, M., Mushotzky, R.F., Angelini, L., Arnaud, K.A., & Quataert, E. 2001, ApJ, 555, 21L
- Maraschi, L., & Tavecchio, F. 2003, ApJ in press (astro-ph/0205252)
- Markoff, S., Falcke, & H. Fender, R. 2001, A&A, 372, 25
- Markowitz, A., & Edelson, R. 2001, ApJ, 547, 684
- Nandra, K., George, I.M., Mushotzky, R.F., Turner, T.J., & Yaqoob, T. 1997, ApJ, 476, 70
- Narayan, R. 2002, Lighthouses of the Universe. Proceedings of the MPA/ESO, ed. M. Gilfanov, R. Sunyaev, & E. Churazov, 405
- Papadakis, I.E., Petrucci, P.O., Maraschi, L., et al. 2002, ApJ, 573, 92
- Pellegrini, S., Venturi, T., Comastri, A., et al. 2003, ApJ, 585, 677
- Petrucci, P.O., Haardt, F., Maraschi, L., et al. 2000, ApJ, 540, 131
- Piner, B.G., Jones, D.L., & Wehrle, A.E. 2001, ApJ, 122, 2954
- Quataert, E. 2003, Astron. Nachr., 324, 3 (astro-ph/0304099)
- Rawlings, S.G., & Saunders, R.D.E. 1991, Nature, 349, 138
- Ross, R.R. & Fabian, A.C., 1993, MNRAS, 261, 74
- Sambruna, R.M., Eracleous, M., & Mushotzky, R. 1999, ApJ, 526, 60
- Sambruna, R.M., Gliozzi, M., Eracleous, M., Brandt, W.N., & Mushotzky, R. 2003, ApJ, 586, 37
- Sarazin C.L., 1988, *X-ray emission from clusters of galaxies*, Cambridge University Press
- Stone, J.M., & Pringle, J.E. 2001, MNRAS, 322, 461
- Tavecchio, F., Maraschi, L., Ghisellini, G., et al. 2000b, ApJ, 543, 535
- Terashima, Y., Iyomoto, N., Ho, Luis C., & Ptak, A.F. 2002, ApJS, 139, 1
- Urry, C.M., & Padovani, P. 1995, PASP, 107, 803
- Vaughan, S., & Edelson, R. 2001, ApJ, 548, 694
- Worrall, D.M., & Birkinshaw, M. 1994, ApJ, 427, 134
- Worrall, D.M., Lawrence, C.R., Pearson, T.J., & Readhead, A.C.S. 1994, ApJ, 420, L17
- Yuan, F., Quataert, E., & Narayan, R. 2003, ApJ submitted (astro-ph/0304125)
- Zdziarski, A.A., Gilfanov, M., Lubiński, P., & Revnivtsev, M. 2003, MNRAS in press (astro-ph/0209363)
- Zhang, Y.H., Celotti, A., Treves, A., et al. 1999, ApJ, 527, 719

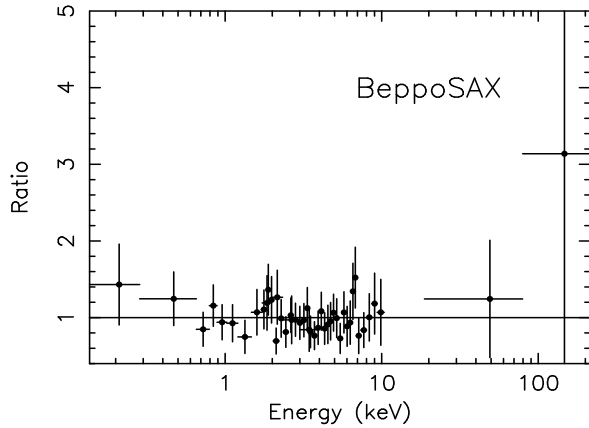
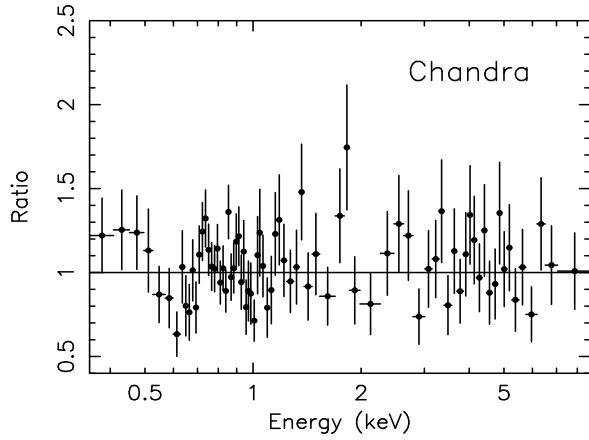
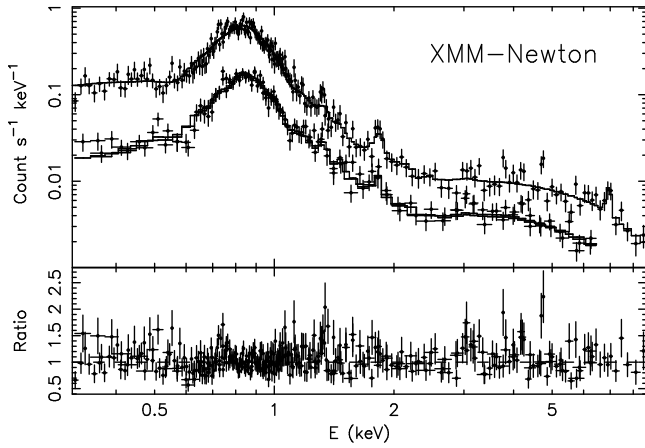


Fig. 5. *Top Panel:* EPIC pn, MOS1, and MOS2 spectra of NGC 4261 with the best-fit model, consisting of a thermal component (`appec` in `XSPEC`), plus a partially covered absorbed power law (`zpcfabs powerlaw`), plus a Gaussian line at ~ 7 keV. The same continuum model fits the *Chandra* and *BeppoSAX* data. *Middle Panel:* Residuals of the best-fit continuum model to the ACIS data. *Bottom Panel:* Residuals of the best-fit continuum model to the *BeppoSAX* LECS+MECS+PDS data.

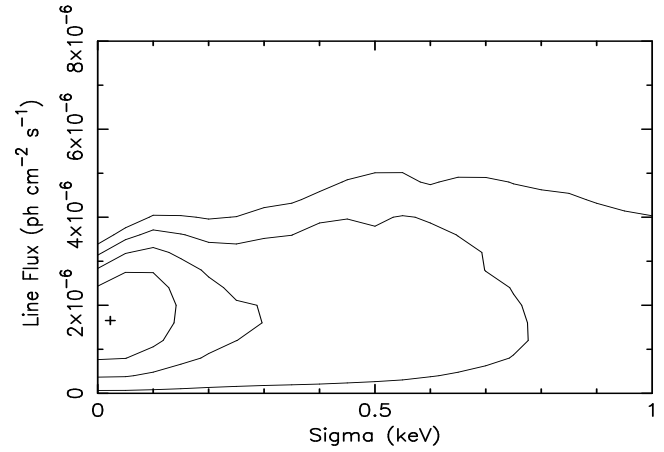


Fig. 6. Confidence contours (68%, 90%, 95%, and 99%) in the σ - line flux plane for the ionized iron line detected with the *XMM-Newton* EPIC pn camera.